

---

# Rapid biomechanical imaging at low irradiation level via dual line-scanning Brillouin microscopy

---

In the format provided by the authors and unedited

---

## Table of Contents

Supplementary note 1	Page 2-3
Supplementary note 2	Page 4-6
Supplementary Fig.1	Page 7
Supplementary Fig.2	Page 8
Supplementary Fig.3	Page 9

## Supplementary note 1: Dual-line illumination configuration

A line-scan configuration in orthogonal geometry, i.e. multiplexed “on-axis” along the illumination beam is highly desirable for rapid detection and low illumination dose (see **Supplementary Note 2**). However, orthogonal microscopy configurations, such as light sheet fluorescence microscopy or on-axis LSBM, carry inherent issues because the illumination and detection paths are affected by the optical property of the sample. Specifically, the index mismatch between sample and medium, the inhomogeneous distribution of the refractive index of the sample and its turbidity will deviate the propagation trajectory of the illumination/detection beams, which causes a decrease of signal intensity and potential distortion of the image. In Brillouin microscopy, this issue also leads to an additional artifact because the value of the Brillouin shift depends on the angle between illumination and collection path, thus a deviation from the orthogonal geometry needs to be carefully considered. To minimize these issues and enable on-axis LSBM, we developed a dual-line illumination configuration, where two beams are counter-propagated and sequentially serve as illumination beams for Brillouin acquisition (**Fig. 1a & 1b, Extended Data Fig. 1**).

The dual line illumination solution comes from both experimental and simulation studies of Brillouin microscopy in orthogonal geometry: we observed that with single-line illumination, there is a noticeable gradient of Brillouin shift along the illumination path due to a deviation from ideal geometry as well as the beam distortion in semi-transparent sample (e.g. **Extended Data Fig. 2a & 2b**). The deviation from orthogonal geometry is mostly caused by two distinct effects: (A) redirection of the illumination beam path; and (B) redirection of the scattered light path. In case A, given the cylindrical shape of the sample holder and the nearly spherical shape of the spheroids, we avoided artifacts in straightforward manner by aligning the illumination beam with the center of the spheroid. As a result, any beam redirection will be restricted to the illumination plane and the orthogonal scattering geometry is maintained. In case B, artifacts are difficult to avoid with single line illumination. The index mismatch between sample and medium as well as the curved sample geometry create a lensing effect that reduces the angle of the scattered light collected by the spectrometer thus introducing a decreasing gradient in Brillouin shift. To quantify the influence of refractive index mismatch, we measured a PDMS sphere (represents homogeneous sample) embedded in 1% agarose gel using dLSBM setup (**Extended Data Fig.3a & 3b, Method**). The Brillouin image of the sphere clearly shows a gradient ( $\sim 0.2$  GHz) along the illumination axis. We then conducted a theoretical calculation to elucidate this effect (**Extended Data Fig.3c**). For a PDMS sphere with radius  $R$ , suppose the illumination beam passes through its center, the distance between the arbitrary point A on the illumination axis and the center of the sphere is

$$d = \frac{R}{\sin(\theta)} \times \frac{n_0}{n_1} \sin(90 - \alpha), \quad (1)$$

where  $\theta$  is the actual scattering angle that is collected by the multiplexed spectrometer with  $90^\circ$  geometry,  $\alpha$  is the azimuthal angle of the sphere,  $n_0$  ( $=1.33$ ) and  $n_1$  ( $=1.43$ ) is refractive index of water and PDMS, respectively. Using the Snell's law, the actual scattering angle  $\theta$  of point A can be determined as

$$\theta = 180 - \alpha - \sin^{-1} \left[ \frac{n_0}{n_1} \sin(90 - \alpha) \right]. \quad (2)$$

The calculated Brillouin shift based on Equation (1) & (2) matched well with the experimental data when the azimuthal angle is in the range of 40°-140° (**Extended Data Fig.3d**). Considering the spheroid as a cluster of cells, we used published value of cellular refractive index ( $n = 1.36$ ) for estimation<sup>1</sup>. In this case, the shift gradient is as much as about 0.06 GHz, which can be corrected before image fusion. We note that the above calculation only works for spherical sample (e.g. spheroid). For biological sample with irregular shape, 3D mapping of the refractive index will be essential for an accurate correction.

Here, we effectively removed this artifact with two illumination beams counter-propagated and overlapped within the field of view. **Extended Data Fig. 2** exemplifies our procedure. Since the artifact always results in a decreased Brillouin shift along propagation direction, we developed a strategy for image fusion after correcting the refractive index induced gradient based on the estimation of theoretical calculation. In case the Brillouin images have observable distortion comparing with the bright-field images, we selected distortion-free part of each image and merge them along illumination axis. The location of the connection is determined by the overall intensity of the Brillouin signal along illumination axis. Alternatively, we adapted a procedure developed in light-sheet microscopy in case the images do not have observable distortion<sup>2</sup>: we optimized co-registration of the single-line illumination images based on the profile features and the bright-field image; next, in the overlapped images, for each pixel we selected the value with larger Brillouin shift to obtain the artifact-free 2D image.

Interestingly, the dual-line illumination is equipped with a translational degree of freedom along the propagation axis so that with illumination NA of 0.1, the field of view of Brillouin imaging along the multiplexed axis can be varied from ~150  $\mu\text{m}$  to ~300  $\mu\text{m}$ . In experiment, we have measured spheroids with diameter of up to ~100  $\mu\text{m}$ ; this limit was set by the penetration depth of the illumination beam due to the turbidity of the spheroids<sup>3</sup>.

For multiplexed spectrometer, the propagation property of Gaussian illumination beam causes the trade-off between multiplexed number and the axial resolution. Briefly, the multiplexed number and the axial resolution is usually determined by the Rayleigh range and beam waist of the illumination light, respectively. Since the Rayleigh range of the Gaussian beam is proportional to the square of the beam waist, increasing multiplexed number will result in decreased axial resolution, and vice versa. However, this trade-off could be mitigated by using different illumination strategies (e.g, focus extension, Bessel beam, etc).

## Supplementary note 2: Total light dose introduced by confocal vs line-scanning configurations for 3D Brillouin imaging

The total energy delivered to a sample depends on the illumination intensity  $I$ , the area of the illumination  $A$ , and the total acquisition time, i.e. the dwell time  $t$  for acquiring one spectrum/voxel times the number of imaged voxels  $N_i$  ( $i = x, y, z$  represents the pixel number in each dimension).

In confocal Brillouin microscopy, to acquire a 3D image, one usually first collects a 2D section ( $N_x \times N_y$  voxels) within the focal plane by point scanning; then moves the focal plane to a different depth in z-direction and collects another 2D section. This strategy is repeated until all the sections ( $N_z$ ) are collected. As a result, the total energy delivered to the sample is:

$$E_{con} = I_{con} \cdot A_{con} \cdot t_{con} \cdot N_x \cdot N_y \cdot N_z \quad (3)$$

The inherent inefficiency of this scanning mechanism is well known: when collecting a voxel in a given plane, the light beam illuminates a large cone of voxels above and below the focal plane.

The line-scanning configuration multiplexes the process of illumination-detection to a line of voxels, thus leading to much quicker image acquisition time. In terms of energy dose, the multiplexing does not necessarily guarantee lower levels because in a linear process, like spontaneous Brillouin scattering, simultaneous acquisition of  $K$  voxels generally requires increasing the illumination intensity by a factor  $K$  to achieve the same SNR at each voxel. However, since spontaneous Brillouin is a weak scattering process (scattering efficiency is about  $10^{-9}$ ), we can effectively operate in non-depletion pump condition, which enables to multiplex many voxels along the incident optical axis without increasing illumination intensity.

To take full advantage of this effect, we aligned the incident beam line along the y direction and thus multiplexed the scanning by 200 folds (**Figure 1a & 1b**). In this scenario, to obtain a 3D image, the beam line needs to be scanned only once in the x direction, and once in z direction (or equivalently at different angles to obtain the 3D volume in spherical symmetry). As a result, the total light dose delivered to the sample is:

$$E_{ls} = I_{ls} \cdot A_{ls} \cdot t_{ls} \cdot N_x \cdot N_z. \quad (4)$$

The ratio of the light dose introduced by two configurations is

$$R = E_{ls}/E_{con} = \alpha/N_y, \quad (5)$$

where  $\alpha = I_{ls}/I_{con} \cdot A_{ls}/A_{con} \cdot t_{ls}/t_{con}$ . In the ideal scenario, both configurations have similar experimental parameters, i.e.  $\alpha = 1$ , and the ratio of the light dose will be simply improved by multiplexed number of voxels along the optical axis  $N_y$ . However, both the illumination areas and the acquisition times per voxel introduce design tradeoffs that need to be evaluated in more depth.

In terms of illumination areas, the two configurations differ because in the confocal epi-detection arrangement the illumination and detection volumes are perfectly overlapped while the 90-degree geometry of line-scanning configuration introduces a mismatch between the size of the incident beam line and the size of the sampled volume. The illumination areas are determined by the numerical apertures (NAs) of the incident beams:  $A_{ls}/A_{con} = NA_{con}^2/NA_{ls-ill}^2$ , where  $NA_{con}$  and

$NA_{ls-ill}$  are the NA of the confocal configuration and the illumination beam of the line-scanning configuration. In our experiment (red line in **Figure 1f**), we created the line scan by focusing a laser beam with a single lens: thus, we used a low illumination NA=0.1 but matched the detection NA (0.3) to the equivalent confocal NA. This lowered the efficiency term of illumination areas, but led to an improved, nearly isotropic, resolution in the line-scan configuration

In terms of acquisition times per voxel, the 90-degree geometry of the line-scanning configuration requires slightly longer collection time because of lower Brillouin geometrical efficiency. The collected Brillouin scattering signal can be written as  $\epsilon = I_{ill} \cdot V \cdot \Omega \cdot S$ , where  $I_{ill}$  is the intensity of the illumination light,  $V$  is the interaction volume of the scattering,  $\Omega$  is the collected solid angle, and  $S$  is the scattering coefficient, which depends on the inherent property of the material and can be considered as a constant here. Thus, the collected scattering signals for confocal and line-scanning configurations are respectively:

$$\epsilon_{con} = I_{con-ill} \cdot S \cdot \pi^2 \cdot 0.61^2 \cdot \lambda^3 / NA_{con}^2, \quad (6)$$

$$\epsilon_{ls} = I_{ls-ill} \cdot S \cdot \pi^2 \cdot 0.61^3 \cdot \lambda^3 / NA_{ls-ill}. \quad (7)$$

With the same illumination intensity ( $I_{con-ill} = I_{ls-ill}$ ) the ratio of the collected scattering power between two configurations is

$$\eta = \epsilon_{ls} / \epsilon_{con} = 0.61 \cdot \frac{NA_{con}^2}{NA_{ls-ill}}. \quad (8)$$

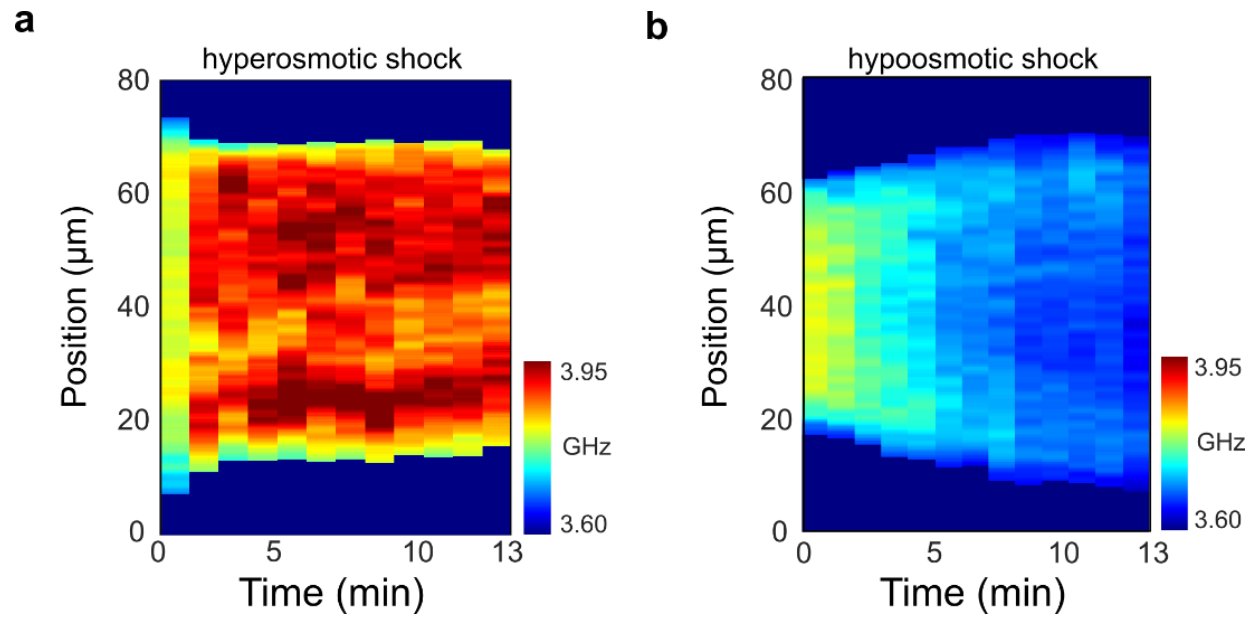
As mentioned, in our line-scanning setup, the illumination NA of our setup is  $NA_{ls-ill} = 0.1$ , while the detection NA is  $NA_{ls-det} = 0.3$ . Considering the confocal setup with same detection NA ( $NA_{con} = 0.3$ ), the ratio of the collected scattering power between two configurations is  $\eta = 0.549$  according to Equation (8). The dwell time is inversely proportional to the collected scattering signal  $t_{ls}/t_{con} = 1/\eta \sim 1.8$ .

Taken together, the expected theoretical value of  $\alpha$  for our configuration is 16.39. This value is consistent with experimental values: Schlüßler et al.<sup>4</sup>, who investigated zebrafish with a confocal configuration at our same wavelength, used laser power of 10 mW, i.e. equivalent laser intensity for NA=0.3 of  $I_{con} = 5.06 \text{ mW}/\mu\text{m}^2$  (note that in confocal configuration, the scattering efficiency is independent of NA) and the exposure time of  $t_{con} = 500 \text{ ms}$ ; this results into an increased efficiency (i.e. experimental value of  $\alpha$ ) of 14.81 compared to our line-scanning geometry. It's important to notice, that the line-scanning configuration can be significantly improved in terms of geometrical efficiency by using focus extension technique; for example, by using the illumination NA of  $NA_{ls-ill} = 0.6$  and maintaining the field-of-view,  $\alpha$  is expected to be 2.7 (black line in **Figure 1f**), suggesting the light dose can be further reduced by about 5 times.

In summary, combining all contributions, the light dose delivered by our line-scanning configuration is 7.4%, i.e. more than one order of magnitude lower than an equivalent confocal configuration, while obtaining 10x speed advantage and 2x improved axial resolution.

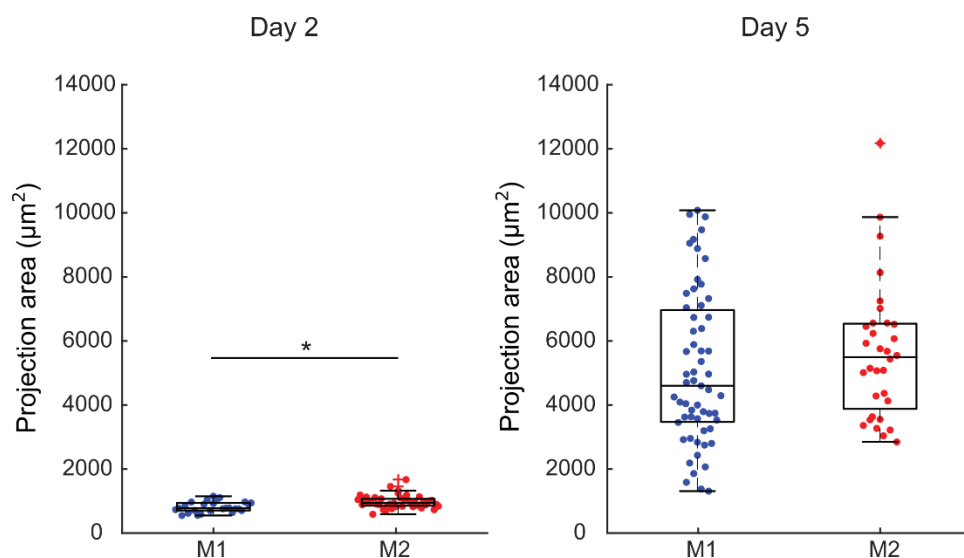
## References

1. Steelman, A., Eldridge, J., Weintraub, B. & Wax, A. Is the nuclear refractive index lower than cytoplasm? Validation of phase measurements and implications for light scattering technologies. *J Biophotonics* 10, 1714-1722 (2017).
2. Huisken, J. et al. Optical sectioning deep inside live embryos by selective plane illumination microscopy. *Science* 305, 1007-1009 (2004).
3. Conrad, C. et al. Mechanical characterization of 3D ovarian cancer nodules using Brillouin confocal microscopy. *Cellular and Molecular Bioengineering* 12, 215-226 (2019).
4. Schlüßler, R. et al. Mechanical mapping of spinal cord growth and repair in living zebrafish larvae by Brillouin imaging. *Biophysical journal* 115, 911-923 (2018).

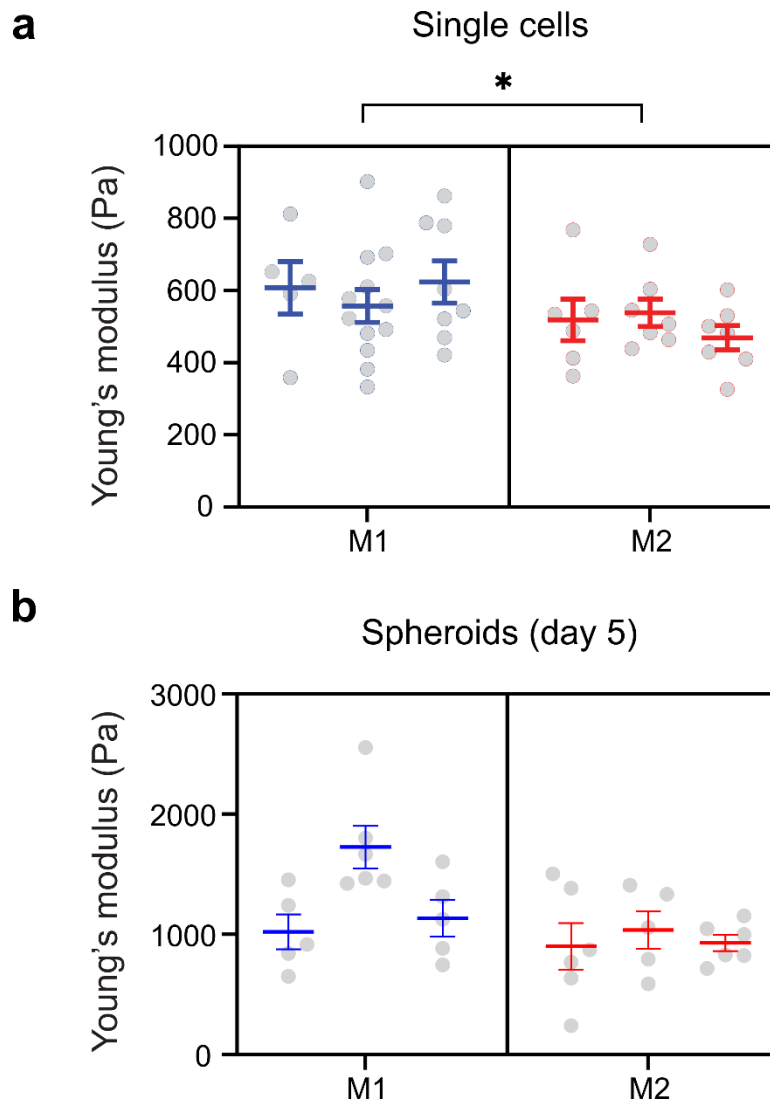


**Supplementary Fig.1:** Spatiotemporal mechanical evolution of spheroid under osmotic shock. Pixels along a vertical line across the center of the spheroids in Fig.2 were analyzed. Time-space Kymograph plots show the mechanical evolution of the spheroids under hyperosmotic shock (a) and hypoosmotic shock (b).





**Supplementary Fig.2:** Evolution of the spheroids' projection area. The averaged areas of M1 and M2 are  $816 \mu\text{m}^2$  and  $978 \mu\text{m}^2$  on Day 2 and increase to  $5125 \mu\text{m}^2$  and  $5624 \mu\text{m}^2$  on Day 5.  $*p=0.0011$ . Statistical significance is determined by performing two-sided two-sample t-test, and no adjustment was made. In all boxplots, the central mark indicates the median, and the bottom and top edges indicate the 25th and 75th percentiles, respectively. The whiskers extend to the most extreme data points not considered outliers.



**Supplementary Fig.3:** All repeats of the Young's modulus measured by AFM. **a**, Indentation measurement on single cells. **b**, Indentation measurement on spheroids of Day 5. The mean  $\pm$  S.E.M is used to represent each repeat. Statistical significance is determined by performing two-sided unpaired t-test with all repeats. \*  $p=0.038$ .